# Insulator roof, acentric absorber tube and nanofluid effect on parabolic trough collector efficiency via two-phase flow simulation

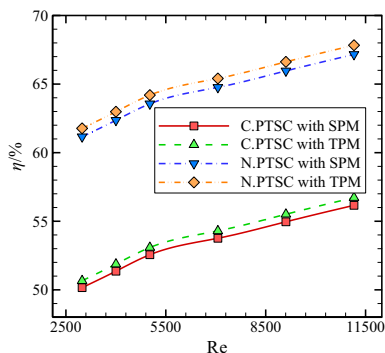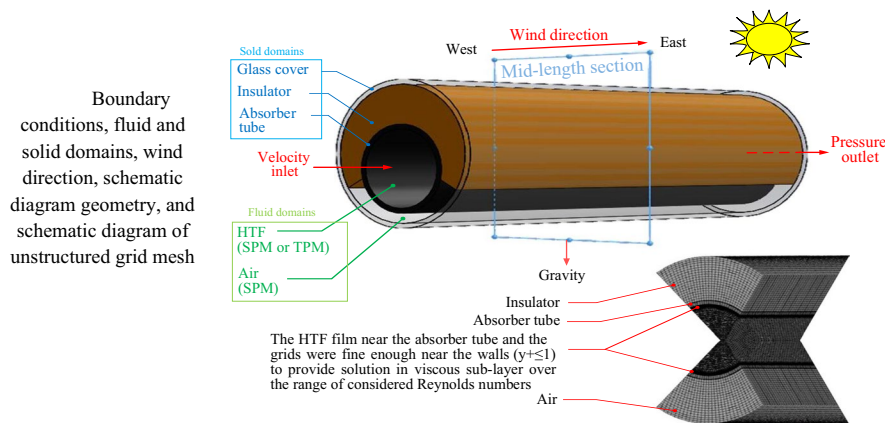Ali Akbar Abbasian Arani[1] · Farhad Monfaredi[1]

## Abstract

Current study aims to present an effectual parabolic trough collector (PTC), which is employed from nanofluid up to 4% as working fluid numerically using the finite volume scheme. Another propose is comparing the responses using the single-phase mixture (SPM) method and two-phase mixture (TPM) method. In this study, the effects of employing acentric absorber tube up to 20mm and an insulator roof from 30° to 150° are investigated. Subsequently, the best arrangement is established. Also, various nanofluid constraints (nanoparticles diameter and volume fraction) for the best arrangement is examined by TPM method. For proposed and conventional PTC configurations, the average Nusselt number by TPM method is higher than by SPM method. Furthermore, it is shown that employing proposed PTC provide higher energy efficiency, Nusselt number, outlet temperature, and performance evaluation criteria (PEC) in studied range of Reynolds numbers from 3000 to 11,500. Finally, the proposed PTC provide the energy efficiency equal to 73.10% having the acentric value of 20mm and arc-angle of 70° occupying by nanofluid considering nanoparticles diameter of 20nm and nanoparticles volume fraction of 1%.

✉ Ali Akbar Abbasian Arani
    abbasian@kashanu.ac.ir

1   Faculty of Mechanical Engineering, University of Kashan,
    Kashan, Iran

## Graphical abstract

Boundary conditions, fluid and solid domains, wind direction, schematic diagram geometry, and schematic diagram of unstructured grid mesh



The HTF film near the absorber tube and the grids were fine enough near the walls (y+≤1) to provide solution in viscous sub-layer over the range of considered Reynolds numbers
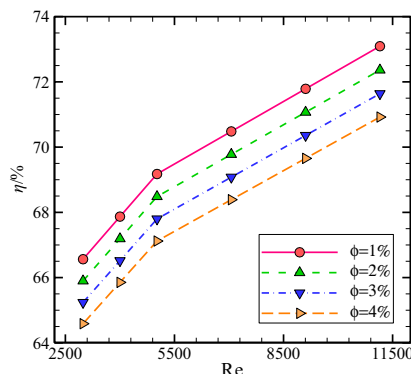


Effects of using SPM and TPM on collector efficiency, for C.PTSC and N.PTSC ($\Lambda = 0$ mm, and $\Psi = 90°$) filled with nanofluid ($\phi = 1\%$ and $d_{np} = 20$ mm)
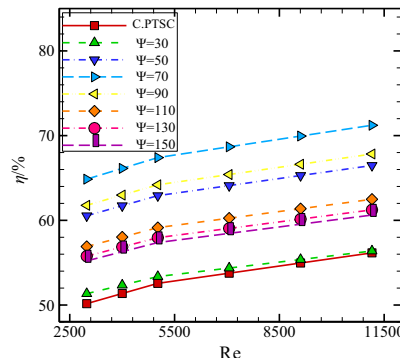


Effects of insulator arc-angles on efficiency for N.PTSC ($\Lambda = 0$ mm) filled with nanofluid ($\phi = 1\%$ and $d_{np} = 20$ mm) and simulated with TPM
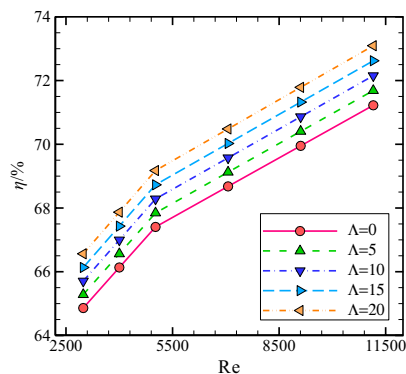


Effects of acentric values on efficiency for the N.PTSC ($\Psi = 70°$) filled with nanofluid ($\phi = 1\%$ and $d_{np} = 20$ mm) and simulated with TPM



Nanoparticles volume fractions effect on efficiency, for N.PTSC ($\Psi = 70°$ and $\Lambda = 20$ mm) filled with nanofluid ($d_{np} = 20$ mm) with TPM

## Abbreviations

| | |
|---|---|
| $A_a$ | Absorber tube surface |
| $\mathcal{A}_{PTSC}$ | Aperture of PTSC |
| $a,$ | Radiation constant ($a = 7.561 \cdot 10^{-19}$ kJm$^{-3}$ K$^{-4}$) |
| $a_i$ | Coefficients in thermal properties of Syltherm 800 oil estimations |
| $C_\mu$ | Standard constant in the turbulent model |
| $c_p$ | Constant specific heat capacity |

| C.PTSC | Conventional PTSC |
|--------|-------------------|
| $D$ | Coefficient of Einstein diffusion |
| $d_a$ | Absorber tube outer diameter |
| $d_g$ | Glass cover outer diameter |
| $d_{np}$ | Nanoparticle mean diameter |
| $e$ | Emission energy |
| $f_{av}$ | Friction factor for enhanced PTSC |
| $f_{av,0}$ | Friction factor for the reference PTSC |
| $G$ | The production rate of $k$ |
| $\vec{g}$ | Fluid gravitational acceleration |
| GM | Gray model |
| HTF | Heat transfer fluid |
| $h_a$ | Convective heat transfer of air-filled annular space |
| $h_g$ | Convective heat transfer of surrounding air with outer glass tube |
| $h_{bf}$ | Base fluid enthalpy |
| $h_s$ | Solid particles enthalpy |
| $I_b$ | Direct normal irradiance |
| $k_{np}$ | Nanoparticle thermal conductivity, |
| $k_{bf}$ | Base fluid thermal conductivity (W m$^{-1}$ K$^{-1}$) |
| $k$ | Thermal conductivity |
| $k_b$ | Boltzmann's constant |
| $L_{PTSC}$ | Length of PTSC |
| $M$ | Molecular mass |
| $N$ | Avogadro number |
| $Nu_{av}$ | Averaged Nusselt number of enhanced PTSC |
| $Nu_{av,0}$ | Averaged Nusselt number of reference PTSC |
| NPTC | Nanofluid based parabolic trough solar collectors |
| N.PTC | Novel PTC |
| $p$ | Pressure |
| Pr | Base fluid Prandtl number |
| $Pr_W$ | Wall temperature Prandtl number |
| PEC | Performance evaluation criterion |
| PTC | Parabolic trough solar collector |
| $\dot{Q}_{rad,r\text{-}a}$ | Transmitted solar irradiance across glass cover by radiation |
| $\dot{Q}_{conv,a\text{-}nf}$ | Heat exchange among heat transfer nanofluid and absorber tube by convection |
| $\dot{Q}_{conv,a\text{-}anna}$ | Heat exchange among absorber tube and annulus-air (anna) by convection |
| $\dot{Q}_{rad,g\text{-}sky}$ | Radiation heat loses with the lower part of the glass cover |
| $\dot{Q}_{rad,a\text{-}sky}$ | Radiation heat loses with the lower part of the absorber tube |
| $\dot{Q}_{cond,a\text{-}ins}$ | Heat exchange among absorber tube and insulation part by conduction |
| $\dot{Q}_{cond,a\text{-}nf}$ | Heat exchange among absorber tube and nanofluid |
| $\dot{Q}_{conv,g\text{-}env}$ | Heat exchange among glass cover and surrounding by convention |
| $Re_{np}$ | Nanoparticle Reynolds number |

| $Re_s$ | Particle Reynolds number |
|--------|------------------------|
| SPM | Single phase model |
| T | Nanofluid temperature |
| $T_a$ | The temperature of air-filled annular space |
| $T_g$ | Surrounding air temperature |
| $T_{a,j}$ | Absorber tube temperature |
| $T_{i,j}$ | Inlet absorber tube fluid temperature |
| $T_{e,j}$ | Exit absorber tube fluid temperature |
| $T_{env}$ | Ambient (environment) temperature |
| $T_{in}$ | Inlet nanofluid temperature |
| $T_{fr}$ | Base fluid freezing point |
| $T_0$ | Surrounding temperature |
| $T_s$ | Surface temperature |
| TPM | Two-phase model |
| $u_B$ | Nanoparticle mean Brownian velocity |
| $\vec{U}_m$ | Mixture velocity or mass-averaged velocity |
| $\vec{U}_s$ | Solid particles velocity |
| $\vec{U}_{bf}$ | The velocity of the base fluid |
| $\vec{U}_{dr,bf}$ | Base fluid drift velocity |
| $\vec{U}_{dr,s}$ | Particles drift velocity |
| $V_w$ | Wind velocity |
| $V_{nf}$ | Nanofluid velocity |

**Greek Symbols**

| $\vec{\alpha}$ | Particle's gravitational acceleration |
|----------------|---------------------------------------|
| $\alpha$ | Absorptance |
| $\delta$ | Half of the sun's cone angle |
| $\delta_a$ | Absorber tube thickness |
| $\delta b$ | Irreversibility of exergy |
| $\varepsilon$ | Emittance |
| $\Lambda$ | Acentric values |
| $\mu$ | Dynamic viscosity |
| $\mu_{t,m}$ | Turbulent viscosity |
| $\mu_m$ | Mixture viscosity |
| $\mu_{eff}$ | Nanofluid viscosity |
| $\sigma_k$ | Standard constants in the turbulent model |
| $\sigma_\varepsilon$ | Standard constants in the turbulent model |
| $\sigma_t$ | Standard constants in the turbulent model |
| $\rho_m$ | Density for a two-phase mixture |
| $\rho$ | Density |
| $\tau$ | Transmittance |
| $\rho_{f0}$ | Base fluid density was evaluated at temperature $T_0 = 293$K. |
| $\tau_D$ | Time request to the distance between two molecules |
| $\varrho$ | Refractive index |
| $\phi$ | Volume fraction |
| $\varsigma_{Rim}$ | Rim angle |
| $\varsigma_{NP}$ | Non-parallelism angle |
| $\psi$ | Highest available solar work |
| $\psi$ | Arc-angle |

# Introduction

Rising energy requirements have accelerated the investigation on the innovative archetypes solar collectors [1, 2] to employing the renewable and sustainable energies [3]. Today, parabolic trough collector (PTC) that are employed in thermic applications and power plants are investigated by a large number of investigators in order to enhance their thermo-hydraulic performance [4–6]. Since the PTCs have more heat absorption than that the other type of collectors, researchers were focused on analyzing the PTCs more and more [7].

Nanofluid-based PTCs (NPTCs), having nanofluid provide higher energy efficiency. It is worth to note that, NPTC can provide average nanofluid temperature higher than absorber tube by smart and accurate design due to direct absorption of irradiance by naofluid [3]. In an investigation by Zaboli et al. [8], a PTC equipped with a helical fins as a swirl generator is analyzed. They reported that employing the hybrid nanofluids show higher heat exchange rate than the water. Also, MWCNT/iron oxide presented the highest thermal performance. In another study by Haran and Venkataramaiah [9] a PTC having $Al_2O_3$/water, $Al_2O_3$/ethylene glycol nanofluids, considering various volume fraction are examined. They showed that employing nanofluid present higher thermal performance than that pure fluid. One can find another investigations in this fields [10–13].

Benabderrahmane et al. [14] presented a study on the convection heat transfer and fluid flow of Alumina/dowtherm-A nanofluid in a PTC having vortex generator employing the two-phase mixture (TPM) method and single-phase mixture (SPM) method. Obtained results demonstrated that TPM method provide higher convection heat transfer coefficient than SPM method, while evaluating friction factor employing TPM and SPM methods are not different.

Osorio and Rivera-Alvarez [15] conducted a study on the characteristics of the PTC having double glass covers. They compared and analyzed the influences of the inner glass tube and vacuum conditions. They reported that a detailed economic and technical study is necessary to provide the total energy cost.

**Table 1** Geometrical characteristics of investigated PTC [31, 32]

| Geometrical constrain | Values |
| --- | --- |
| PTC length, $L_{PTSC}$ | 4.06 m |
| Absorber tube outer diameter, $d_a$ | 0.07 m |
| Absorber tube thickness, $\delta_a$ | 0.003 m |
| Glass tube outer diameter, $d_g$ | 0.12 m |
| PTC aperture, $A_{PTSC}$ | 0.525 m |
| Rim angle, $\varsigma_{Rim}$ | 15° |
| Non-parallelism angle, $\varsigma_{NP}$ | 16′ |

Also by utilizing proposed methods, one can obtain higher collector efficiency, especially at higher temperatures. Khosravi et al. [16] perform a study on the magnetic field influences numerically on the heat transfer augmentation in a PTC having the Ferro nanofluids ($Fe_3O_4$-Therminol 66). The obtained result confirmed that existence of magnetic field could improve the heat transfer coefficient, thermal efficiency, and PTC outlet fluid temperature. Liu et al. [17] conducted an investigation for the entropy generation and PTC performance equipped with a conical strip. They showed that the heat transfer improves sharply employing the conical strip. In addition, the Nusselt number presents an enhancement equal to 203%. Sadeghi et al. [18] presented a numerical/experimental study on the evacuated PTC performance having the synthesized $Cu_2O$/distilled water nanofluid as working fluid. They show that the energy and exergy efficiency improve 10 and 12.7%, respectively, with utilization of nanofluid as working fluid. Wang et al. [19] presented the proposal of installing an insulator roof overhead the absorber tube inside the PTCs for thermal losses reducing to 24%. Yang et al. [20] recommended a PTC, which utilizes different coatings in the lower and upper sections of the absorber tube. They founded that this technique could diminish the thermal loss by more than 30%. In the other study, Al-Ansary and Zeitoun [21] employed this technique with air inside the tube cavity. They showed that employing this technique in the PTC will improve the efficiency and reduce heat loss. Hanafizadeh et al. [22] presented an investigation on the utilization of SPM and TPM

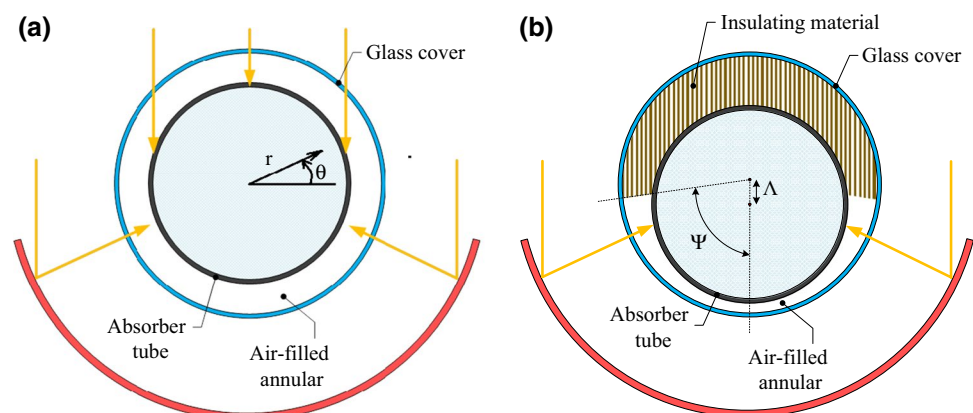**Fig. 1** **a** C.PTC (conventional PTC), and **b** N.PTC (novel PTC)

**Table 2** Stainless-steel and Pyrex glass thermo-physical properties [33]

| Property | Symbol /unit | Pyrex glass | Stainless steal | Glass-wool | γ-AIOOH | Air |
|---|---|---|---|---|---|---|
| Transmittance | $\tau$/– | 0.95 | – | – | – | – |
| Refractive index | $\varrho$ /- | 1.474 | – | – | – | – |
| Absorptance | $\alpha$/- | – | 0.96 | – | – | – |
| Emittance | $\varepsilon$/- | – | 0.14 | – | – | – |
| Density | $\rho$/kg m$^{-3}$ | $2.23 \cdot 10^{-3}$ | 7920 | 18 | 3050 | 1.125 |
| Specific heat | $c_{\mathrm{p}}$/J kg$^{-1}$ K$^{-1}$ | 750 | 444 | 670 | 618.3 | 1006.43 |
| Thermal conductivity | $k$/W m$^{-1}$K$^{-1}$ | 1.14 | 16 | 0.04 | 30 | 0.0242 |
| Dynamic viscosity | $\mu$/Pa s | – | – | – | – | $1.789 \cdot 10^{-5}$ |

**Table 3** Syltherm 800 correlations constant [34]

| Property | $\rho$ /kg m$^{-3}$ | $c_{\mathrm{p}}$ /J kg$^{-1}$K$^{-1}$ | $k$ /W m$^{-1}$K$^{-1}$ | $\mu$ /Pa s |
|---|---|---|---|---|
| $a_0$ | $1.26903060 \cdot 10^3$ | $1.10787577 \cdot 10^3$ | 0.19011994 | $8.486612 \cdot 10^{-2}$ |
| $a_1$ | $-1.52080898$ | 1.70742274 | $-1.88022387 \cdot 10^{-4}$ | $-5.54127710 \cdot 10^{-4}$ |
| $a_2$ | $1.79056397 \cdot 10^{-3}$ | 0 | 0 | $1.388285 \cdot 10^{-6}$ |
| $a_3$ | $-1.67087252 \cdot 10^{-6}$ | 0 | 0 | $-1.566003 \cdot 10^{-9}$ |
| $a_4$ | 0 | 0 | 0 | $6.672331 \cdot 10^{-13}$ |

methods in a tube with magnetic field for forced convection flow regime employing the nanofluid as working fluid. Amani et al. [23] studied numerically the influences of nanoparticle distribution, employing TPM method, for nanofluid turbulent flow regime. The effects of Peclet number, Reynolds number, diameter of nanoparticles, and nanoparticles volume fraction have been examined. Kumar and Sarkar [24] investigated numerically on the performances of hybrid nanofluid flowing in a minichannel heat-sink by TPM method in a laminar flow and forced convection heat transfer. Khosravi-Bizhaem and Abbassi [25] investigated the influence of curvature in forced convection on the nanofluid entropy generation inside the helical coil by TPM method. Alsarraf et al. [26] investigated boehmite alumina/water-EG nanofluid performance of turbulent flow having various morphology of nanoparticle in a heat exchanger employing TPM method. In referred investigation, the effects of Reynolds number, nanoparticles volume fraction, and morphology on performance were studied. Mohammed et al. [27] present a study on the nanofluid fluid flow and force convective heat transfer as working fluid in a circular tube having a convergent/divergent conical ring as turbolator by TPM method. Barnoon et al. [28] provided a numerical investigation on the nanofluid flow entropy production between two concentric tubes considering magnetic field by TPM and SPM methods. They demonstrated that Nusselt number using TPM method is higher than using SPM method, and the maximum pressure drop using SPM and TPM methods occurred at the highest nanoparticles volume fractions and maximum Hartman number. Investigation on this field are presented [29] and extended [30] by a large number of researchers.

The literature assessment reveals that, although the half-insulated in PTC influences has been studied, there is not any study that employs the acentric absorber tube and insulator roof considering different arc-angles for a PTC utilizing the nanofluid as working fluid by the TPM method to study the influences of the related parameter on the collector efficiency. Due to presented reason, the first objective of this investigation is to presenting a comparison between the results obtained by SPM and TPM methods in the PTC employed the nanofluid as working fluid. The second objective is to present an optimize PTC having the nanofluid. The influences of employing the SPM and TPM methods on the nanofluid flowing flow and heat transfer through absorber tube are studied as the first goal, and then the consequences of utilizing the insulator roof are investigated. The consequences of utilizing an acentric absorber tube as the next
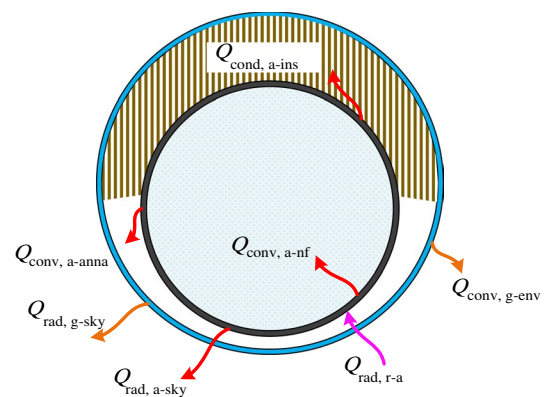


**Fig. 2** Novel PTC heat transfer mechanisms

goal are presented. Accordingly, in referred step, the optimal arrangement is established, and as the last and main aim of the current study, the nanofluid parameters influences on the obtained (as optimum) configuration are studied by TPM method. To accomplish these objects, the results for the Nusselt number, pressure drop, friction factor, energy efficiency, PEC, and outlet temperature are provided and discussed.

## Physical model

### Model presentation

Figure 1 shows the C.PTC (conventional PTC) and N.PTC (novel PTC) considering acentric absorber tube and insulator roof. It must note that for two referred PTC (conventional and proposed) the annulus, installed between the glass cover and absorber tube, has air with pressure equal to 0.83 atm. The principal idea is to establish an insulating material in the annulus air, and obtaining the optimal insulator roof arc-angle. In the referred case via employing the acentric absorber tube, utilizing further insulator material volume overhead of the absorber tube leads to reducing the heat loss. As it shown in Fig. 1b, the proposed collector has an absorber tube accompanied with a coating (a glass tube), an air-filled annulus with an insulator roof, which is installed in the upper part of the annulus. As it shown by Fig. 1, the solar radiation is reflected and concentrated by the reflector, and the reflected solar energy goes through the glass window and to be received with the absorber tube due to employing a special absorption coating.

Table 1 presents the detailed geometrical aspect of PTC. In the present study two essential geometrical constraints will be optimized by energy efficiency which are acentric value ($\Lambda$) and insulator arc-angle ($\Psi$).

Various arc-angle varies from $\Psi = 30°$, to $\Psi = 150°$, consisting seven values, different acentric values varies from $\Lambda = 0$ to $\Lambda = 20$mm consisting five values, and various mass flow rate from 0.107 to 0.535 kg s$^{-1}$ that correspond to the Reynolds number from Re = 2985.9 to Re = 11,151.6 are examined.

The wind velocity is $V_w = 2.5$ m s$^{-1}$, the employed direct normal radiation is $I_b = 1000$W m$^{-2}$, the inlet nanofluid temperature is selected equal to $T_{in} = 300$K, and the temperature of environment is equal to $T_{env} = 297.5$K.

The glass tube is made from the Pyrex glass anti-reflective coated, and its thermophysical properties are presented in Table 2. Stainless-steel is used for absorber tube accompanies a special surface, and its physical properties are provided in Table 2. In addition, the annulus has the air, and the glass-wool is used as insulator material, Table 2, Sadripour [33]. The Syltherm 800 oil is employed as working fluid, and the following equation is utilized in order to estimate the thermophysical properties, Dudley et al. [34]:

$$f(T) = a_0 + a_1 T + a_2 T^2 + a_3 T^3 + a_4 T^4, \tag{1}$$

where $T$ refers to the temperature of working fluid (K). It must note that used equation, $f(T)$, can be temperature dependent density, specific constant pressure heat capacity, dynamic viscosity, and thermal conductivity coefficient.

Corresponding values of used coefficients of the presented equation are provided by Table 3. Referred correlation is utilized for the temperature between the 300–650 K.

In the current investigation, boehmite-alumina ($\gamma$-AlOOH) as nanoparticle is employed, and corresponding thermophysical properties are presented by Table 2. In addition, the thermophysical properties of employed nanofluid (Syltherm 800 oil/$\gamma$-AlOOH) are evaluated via Eqs. (2)–(10).

The nanofluid density, $\rho_{nf}$, and constant pressure heat capacity, $c_{P,nf}$, for each section-temperature $(T_m)$ are evaluated by mixture relation.

With accounting nanoparticles Brownian effect, the nanofluid thermal conductivity coefficient ($k_{eff}$) be calculated by Corcione equation [35]:

$$\frac{k_{eff}}{k_{bf}} = 1 + 4.4 Re_{np}^{0.4} Pr_{bf}^{0.66} \phi^{0.66} \left(\frac{T}{T_{fr}}\right)^{10} \left(\frac{k_{np}}{k_{bf}}\right)^{0.03}, Re_{np} = \frac{\rho_{bf} u_B d_{np}}{\mu_{bf}}, \tag{2}$$

where $Re_{np}$ mentions the nanoparticles Reynolds number, Pr denotes to the Prandtl number of base fluid, $T$ mentions to the temperature of nanofluid, $T_{fr}$ denotes to the freezing point of base fluid, $k_{np}$ mentions to the thermal conductivity coefficient of nanoparticles, and $\phi$ denotes to the volume fraction. In nanoparticles Reynolds number, $\mu_{bf}$ and $\rho_{bf}$ are the base fluid dynamic viscosity, and base fluid density, respectively, and $u_B$ and $d_{np}$ are the nanoparticles Brownian velocity and nanoparticles diameter, respectively.

$u_B$ is the ratio among $d_{np}$ and the time $\tau_D$ necessary to traverse such distance (Keblinski et al. [36]) is:

$$\tau_D = \frac{d_{np}^2}{6D} = \frac{\pi \mu_{bf} d_{np}^3}{2k_b T}, u_B = \frac{2k_b T}{\pi \mu_f d_{np}^2}, \tag{3}$$

where $D$ and $k_b$ are *Einstein and Boltzmann's constants. The*refore $Re_{np}$ is:

$$Re_{np} = \frac{2\rho_{bf} k_b T}{\pi \mu_{bf}^2 d_{np}}, \tag{4}$$

where the nanofluid thermophysical properties are calculated at the temperature of nanofluid.

Dynamic viscosity [35]:

$$\frac{\mu_{\text{eff}}}{\mu_{\text{bf}}} = \frac{1}{1 - 34.87\left(\frac{d_{\text{np}}}{d_{\text{bf}}}\right)^{-0.3}\phi^{1.03}}, d_{\text{bf}} = 0.1\left(\frac{6M}{N\pi\rho_{\text{f0}}}\right)^{1}/3,$$

(5)

where $d_{\text{bf}}$ is the base fluid molecule equivalent diameter. $M$ is the base fluid molecular weight, $N$ denotes to the Avogadro number, and $\rho_{\text{f0}}$ is the base fluid density estimated at reference temperature $T_0 = 293\text{K}$.

## Energy balance

Syltherm 800 oil/$\gamma$-AlOOH nanofluid is used as heat transfer fluid (HTF). Various heat exchange mechanism is take place inside the PTC that are illustrated in Fig. 2. As it is displayed, reflected solar radiation concentrate on the PTC, heat exchange between the reflector and absorber tube by radiation transmitted via glass cover ($\dot{Q}_{\text{rad,r}-a}$), heat transfer among the HTF and absorber tube by convection ($\dot{Q}_{\text{conv,a}-\text{nf}}$), natural convection among the annulus-air (anna) and absorber tube ($\dot{Q}_{\text{conv,a}-\text{anna}}$), heat exchange between the glass cover, absorber tube and sky via radiation ($\dot{Q}_{\text{rad,g}-\text{sky}}$) and ($\dot{Q}_{\text{rad,a}-\text{sky}}$), heat exchange between the insulation part and the absorber tube via conduction ($\dot{Q}_{\text{cond,a}-\text{ins}}$), and heat exchange between the glass cover and ambient air via convection ($\dot{Q}_{\text{conv,g}-\text{env}}$). Heat loss due to conduction from the upper part is ignored [37]. Heat exchange with the environment (heat loss) happens by the convection and radiation mechanisms. Referred type of convection heat transfer among the glass cover and surrounding is identified by wind velocity situations. Subsequent assumptions are used in the numerical simulation [38]:

- Radiation heat exchange for the infrared spectrum approaches to zero.
- Used glass tube is very thin, and hence the solar irradiance absorption by the glass tube is ignored.
- The pressure variation inside the absorber tube is low, so the nanofluid and airflow are assumed to be steadystate and incompressible conditions.
- Different edges are assumed to be in adiabatic condition considering zero heat loss.

Heat exchange between the annulus (the insulated section) and other part is considered with the following equation [38]:

$$\frac{A}{2}\rho_{\text{nf}}c_{\text{p,nf}}\frac{dT_{\text{nf}}}{dt} = -\dot{m}\frac{d}{dz}\left(c_{\text{p,nf}}T_{\text{nf}} + \frac{V_{\text{nf}}^2}{2}\right) + Q_{\text{conv,a-nf}},$$

(6)

where $Q_{\text{conv,a}-\text{nf}}$, is evaluated by Eq. (12), while the Nusselt number is evaluated by the equation provided in the literature as [39–41]:

$$Q_{\text{conv,a}-\text{nf}} = \pi\text{Nu}_{\text{nf}}k_{\text{nf}}(T_a - T_{\text{nf}}),$$

(7)

$$\text{Nu}_{\text{nf}} = \frac{\frac{\mathcal{F}_{\text{ann}}}{8}\text{RePr}}{\mathcal{K} + 12.7\sqrt{\frac{\mathcal{F}_{\text{ann}}}{8}}\left(\text{Pr}^{2/3} - 1\right)}\left(1 + \left(\frac{d_{\text{h}}}{L}\right)^{2/3}\right)\mathbb{F}_{\text{ann}}\mathbb{K}.$$

(8)

Detail of presented relation is provided in related reference [40].

Two heat exchange mechanisms between the glass cover and the absorber tube happen, natural convection that presented by the following equation, and radiation, which is calculated via view factors evaluation [42]. Coefficient of natural convective ($h_a$) for the airfilled has been provided as follows [43]:

$$Q_{\text{conv,a}-\text{anna}} = h_a\pi d_a(T_a - T_g).$$

(9)

The heat exchange between the glass cover and ambient air is via convection and radiation heat transfer. Moreover, two types of convection losses exist, natural convection (when the wind velocity is not considerable) and forced convection (when the wind velocity is considerable). Heat loss due to convection having significant wind velocity is as follows.

$$Q_{\text{conv,g}-\text{env}} = h_g\pi d_g(T_g - T_{\text{env}}), h_g = \frac{\text{Nu}_g k_g}{d_g},$$

(10)

where ($h_g$) is the coefficient of convective heat transfer.

The Nusselt number is presented by the subsequent correlation [44]:

$$\text{Nu}_g = c\text{Re}_D^m\text{Pr}^\eta\left(\frac{\text{Pr}}{\text{Pr}_w}\right)^\varpi,$$

(11)

where $m$ and $\eta$ are obtained from the reference, [44]. The value of $\varpi$ determined by the direction of heat flux: $\varpi = 0.25$ is recommended for HTF [39, 44].

## Governing equations

Syltherm 800 oil/$\gamma$-AlOOH nanofluid flow inside the PTC are simulated employing two methods. The first one, which will be used for validation, is the SPM method (in section "Validation results") for air simulation inside the annulus, which assumes that both nanoparticles ($\gamma$-AlOOH) and base fluid (Syltherm 800 oil) have the identical temperature distribution and velocity field. Hence, the system of governing equations may be discretized as if the nanofluid is assumed a *Newtonian* fluid using the suspension thermophysical properties. The other (second) method is based on the (*Eulerian-Eulerian*) single fluid by TPM method, having strong coupling among the phases, and assuming that the particles closely follow the

suspension (mixture) flow. The solid nanoparticles and fluid have been assumed to be inter-penetrating, and it is presumed that each phase possess its specific velocity. The proposed method is presented to obtain powerful estimations even for low volume fractions [45]. The system of governing equation including continuity, energy and, momentum equations for the suspension (nanofluid) are employed as an alternative of using the governing equations of each phase separately (fluid and solid) [46]. The system of governing equations, including energy, momentum, and continuity equations are:

$$\vec{\nabla}\left(\rho_m \vec{U}_m\right) = 0, \tag{12}$$

$$\rho_m\left(\vec{U}_m \vec{\nabla} \vec{U}_m\right) = -\vec{\nabla}p + \mu_m\left(\vec{\nabla} \vec{U}_m + \left(\vec{\nabla} \vec{U}_m\right)^T\right) \\ + \vec{\nabla}\left(\rho_{bf}\phi_{bf}\vec{U}_{dr,bf}\vec{U}_{dr,bf} + \rho_s\phi_s\vec{U}_{dr,s}\vec{U}_{dr,s}\right) + \rho_m \vec{g}, \tag{13}$$

$$\vec{\nabla}\left(\rho_{bf}\phi_{bf}\vec{U}_{bf}h_{bf} + \rho_s\phi_s\vec{U}_s h_s\right) = \vec{\nabla}\left(\left(\phi_{bf}k_{bf} + \phi_s k_s\right)\vec{\nabla}T\right). \tag{14}$$

In system of governing equation, $\vec{U}_m$ denotes to the velocity of mixture, $\rho_m$ denotes to the two-phase mixture density, $\vec{U}_{dr,bf}$ and $\vec{U}_{dr,s}$ mention to the base fluid and particles drift velocity, respectively, and are calculated as [45, 46]:

$$\vec{U}_m = \frac{\rho_s\phi_s\vec{U}_s + \rho_{bf}\phi_{bf}\vec{U}_{bf}}{\rho_m}, \tag{15}$$

$$\rho_m = \rho_s\phi_s + \rho_{bf}\phi_{bf}, \tag{16}$$

$$\vec{U}_{dr,bf} = \vec{U}_{bf} - \vec{U}_m, \tag{17}$$
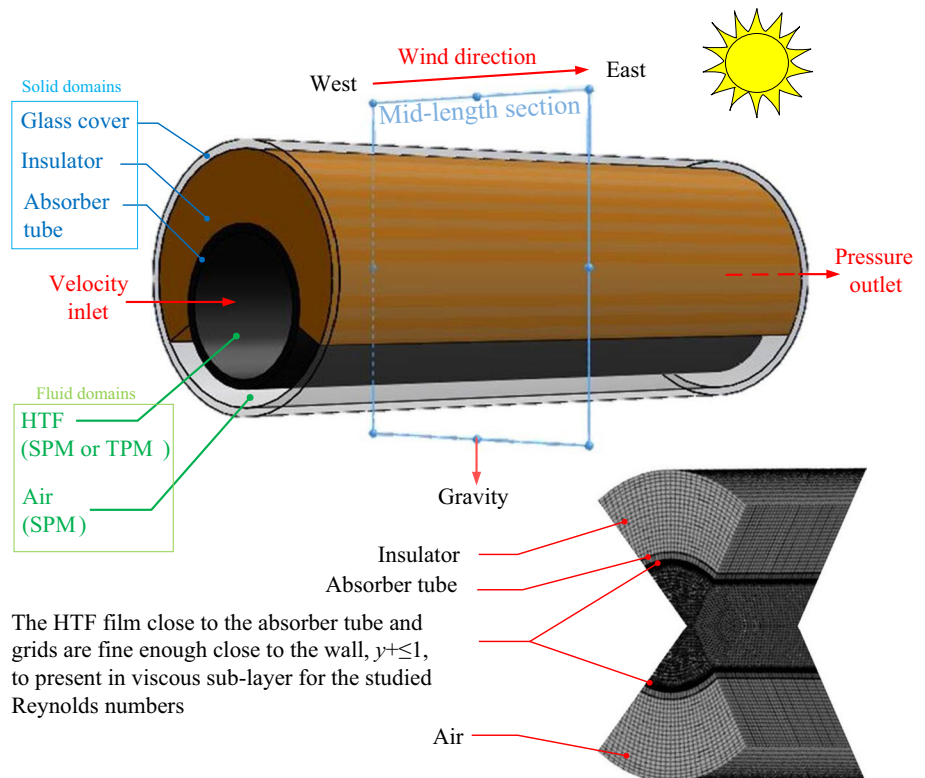
$$\vec{U}_{dr,s} = \vec{U}_s - \vec{U}_m, \tag{18}$$

where $\vec{U}_s$ refers to the solid particles velocity, $\vec{U}_{bf}$ mentions to the base fluid velocity. In addition, $p$ mentions the pressure, $\mu_m$ denotes to the mixture viscosity. In energy conservation equation $h_s$ and $h_{bf}$ are the solid particles and base fluid enthalpy, respectively.

Volume fraction equation is as:

**Table 4** Results of grid independence study

| Test no. | Grid no. | $T_{out}$/°C | Error/% |
|---|---|---|---|
| 1 | 462,727 | 84.458 | 15.5 |
| 2 | 856,009 | 71.358 | 6.27 |
| 3 | 1,365,347 | 66.873 | 9.27 |
| 4 | 2,124,817 | 60.670 | 3.96 |
| 5 | 2,721,873 | 58.274 | 0.03 |
| 6 | 2,933,289 | 58.257 | – |

**Fig. 3** Geometry, solid and fluid domains, wind direction, boundary conditions, and unstructured grid mesh



The HTF film close to the absorber tube and grids are fine enough close to the wall, $y+\leq1$, to present in viscous sub-layer for the studied Reynolds numbers

$$\vec{\nabla}\left(\rho_s \phi_s \vec{U}_m\right) = -\vec{\nabla}\left(\rho_s \phi_s \vec{U}_{dr,s}\right). \tag{19}$$

The slip velocity is written as:

$$\vec{U}_{bf,s} = \vec{U}_{bf} - \vec{U}_s, \tag{20}$$

and the equation connecting the drift velocity and relative velocity can be presented as [45, 46]:

$$\vec{U}_{dr,s} = \vec{U}_{s,bf} - \frac{\rho_s \phi_s}{\rho_m} \vec{U}_{bf,s}. \tag{21}$$

The relative velocity is defined with Schiller and Naumann [47] as:

$$\vec{U}_{bf,s} = \frac{d_p^2}{18\mu_{bf} f_d} \frac{\rho_s - \rho_m}{\rho_s} \vec{\alpha}, \tag{22}$$

$$f_d = 1 + 0.15 Re_s^{0.687}, \tag{23}$$

$$\vec{\alpha} = \vec{g} - \left(\vec{U}_m \vec{\nabla} \vec{U}_m\right), \tag{24}$$

where $\vec{\alpha}$ and $\vec{g}$ mention to the particle and fluid gravitational acceleration, respectively. The Reynolds number of the particle ($Re_s$) is evaluated as:

$$Re_s = \frac{\rho_m d_p \vec{U}_m}{\mu_m}, \tag{25}$$

where $d_p$ mentions the mean diameter of the particle, here it is equal to 38 nm.

Fluid flow of HTF inside the absorber tube is presumed located in turbulent flow (Re > 2300). The $k$–$\varepsilon$ turbulence

model has been used in ANSYS-Fluent commercial software. Choosing the $k$–$\varepsilon$ model is permitting to its extensive acceptance since this is successfully used in a large number of similar numerical studies inside the PTCs [48–50]. The temperature-dependent properties of the HTF are considered in the present simulations. The equations which provide the $k$–$\varepsilon$ model are defined as follows:

$$\vec{\nabla}\left(\rho_m \vec{U}_m k\right) = \vec{\nabla}\left(\left(\mu_m + \frac{\mu_{t,m}}{\sigma_k}\right)\vec{\nabla}k\right) + G_{k,m} - \rho_m \varepsilon, \tag{26}$$

$$\vec{\nabla}\left(\rho_m \vec{U}_m \varepsilon\right) = \vec{\nabla}\left(\left(\mu_m + \frac{\mu_{t,m}}{\sigma_\varepsilon}\right)\vec{\nabla}\varepsilon\right) + \frac{\varepsilon}{k}\left(c_1 G_{k,m} - c_2 \rho_m \varepsilon\right), \tag{27}$$

where the $\mu_{t,m}$ mentions to turbulent viscosity and $k$, $G$ refer to the production rate are given by [38–50]:

$$\mu_{t,m} = C_\mu \rho_m \frac{k^2}{\varepsilon}, \tag{28}$$

$$G_{k,m} = \mu_{t,m}\left(\vec{\nabla}\vec{U}_m + \left(\vec{\nabla}\vec{U}_m\right)^T\right). \tag{29}$$

Here the empirical constants are used, $c_1 = 1.44$, $c_2 = 1.92$, $C_\mu = 0.09$, $\sigma_k = 1.00$, $\sigma_\varepsilon = 1.30$ and $\sigma_t = 0.85$.

Radiation heat exchange simulation in the annulus tube has been considered by the Monte Carlo method, whereby the radiation be assumed to affect the medium by heating the domain surface, with no energy transmission to the medium (it is called S2S, *Surface-to-Surface*). Referred assumption is trustworthy since the annulus has been assumed with low-pressure air (under 0.83 atm), as it is stated in section "Model presentation". Gray Model (GM) is selected, which determines all radiation quantities uniform in the spectrum. Some used parameters are presented as follows. Fluid flow Reynolds number is evaluated as:

$$Re = \frac{\rho_{bf} u_m d_a}{\mu_{bf}}, \tag{30}$$

$$Nu = \frac{h_{bf} d_a}{k_{bf}}, \tag{31}$$

where $u_m$ mention the velocity of the fluid inside the test section. In addition, $h_{bf}$ and $k_{bf}$ illustrate the base fluid heat transfer coefficient and base fluid coefficient of thermal conductivity, respectively.

The pressure drop among the outlet and inlet, and the friction factor is calculated as:

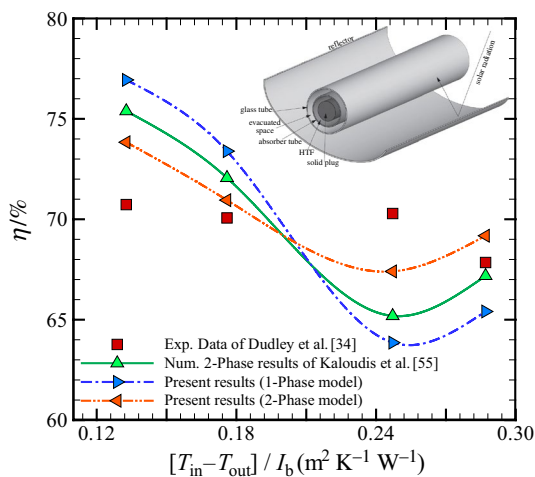$$\Delta p = p_{av,inlet} - p_{av,outlet}, \tag{32}$$



**Fig. 4** Code validation, comparison among the obtained results (SPM and TPM methods), with numerical results [55] and experimental data [34]

**Fig. 5** SPM and TPM methods effects on **a** average Nusselt number, **b** pressure drop, **c** mean friction factor, **d** PEC, **e** PTC outlet temperature, and **f** overall collector efficiency, with Reynolds number for N.PTC and C.PTC ($\Psi = 90°$ and $\Lambda = 0$mm) having nanofluid ($d_{np} = 20$mm and $\phi = 1$%)
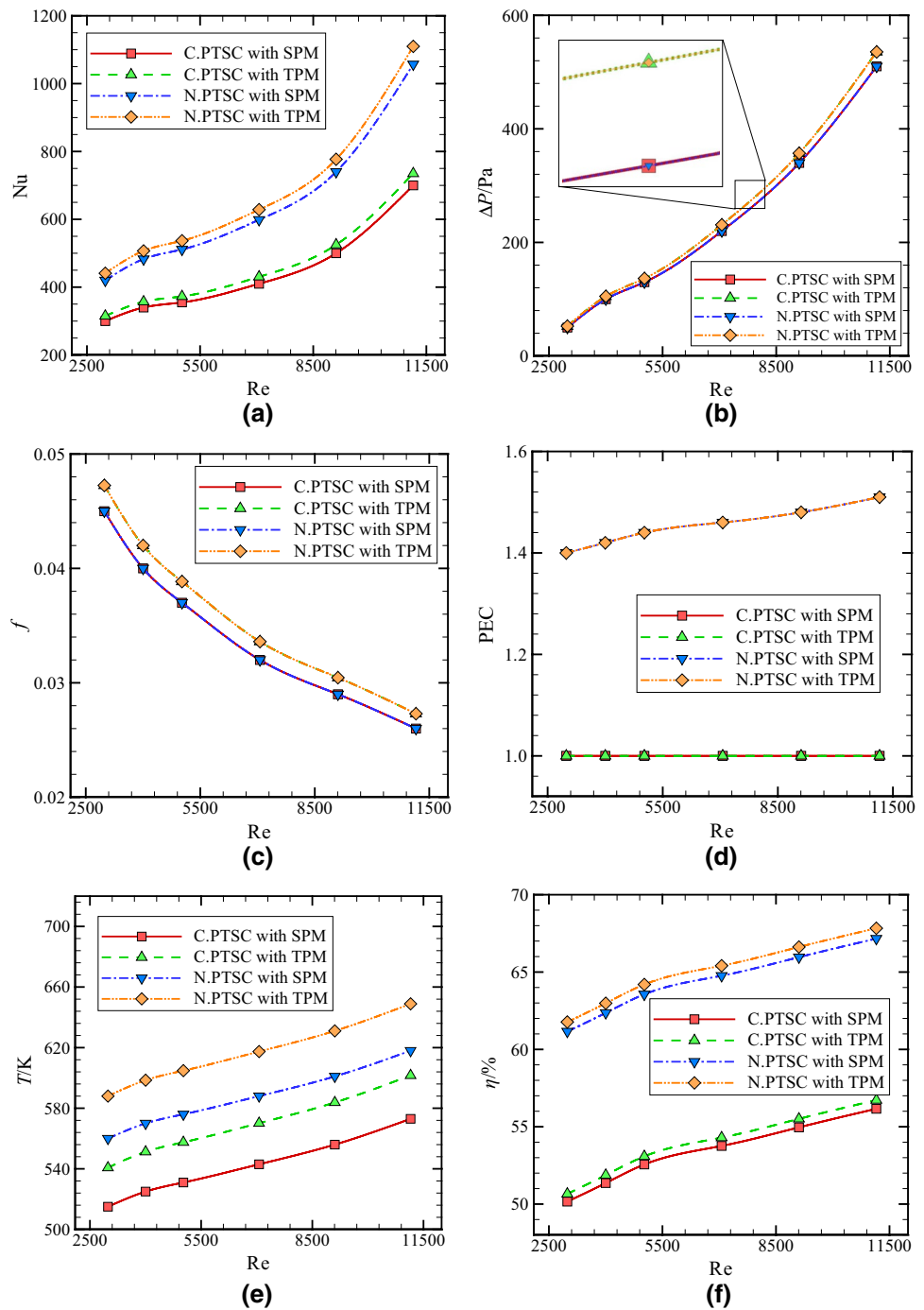
$$f = \frac{2}{\left(\frac{L}{d_a}\right)} \frac{\Delta p}{\rho_{nf} u_m^2}. \tag{33}$$

The performance evaluation criterion index (PEC) is employed to check the solar heat exchanger performances employing nanofluid to evaluate the actual heat transfer development. It is evaluated using the evaluated Nusselt number and friction factor as [51–55]:

$$PEC = \left(\frac{Nu_{av}}{Nu_{av,0}}\right) \cdot \left(\frac{f}{f_0}\right)^{-1/3}, \tag{34}$$

where $Nu_{av}$ and $Nu_{av,0}$ refer to the investigated and reference PTC Nusselt number, respectively. Also, $f$ and $f_0$ refer to the investigated and reference PTC friction factor, respectively. For conventional collector, the collector efficiency, $\eta_c$, as an important index presenting the capability of the collector

to convert the solar radiation into thermal energy may be calculated as:

$$\eta_c = \frac{E_c}{IA} = \frac{Q_{in}\rho_{in}c_{p,in}(T_{out} - T_{in})}{6 * 10^4 IA}. \quad (35)$$

### The boundary conditions equations

Figure 3 presents the schematic diagram (for proposed (Novel) PTC (N.PTC) considering acentric value of 15mm, and arc-angle of 50°), solid and fluid domains, wind direction, the boundary conditions, and unstructured grid (for Conventional PTC (C.PTC) considering acentric value of 0mm, and arc-angle of 90°). As is shown in this figure, the grids in the HTF film close to the absorber tube surface are adequate fine ($y+ \leq 1$) to present the solution in viscous sub-layer.

### Validation results

As is presented by Table 4, a grid investigation was accomplished with the conventional collector employing water to analyze the grid size influences on the obtained results. As is shown, this study are done through the six sets of grid. With comparing the obtained results, one can find that the mesh configurations contain a grid number equal to 2,933,289 nodes is determined to an acceptable resolution between the accuracy and computational time having 0.03 percent as the maximum error. In addition, the insulator part between the absorber tube and glass cover is meshed and simulated with uniform grid. Furthermore, close to the wall finer grids were used to capture the boundary layer (including viscous sub-layer) carefully. Figure 3 presents a view from employed grid.

In addition, validation procedure was accomplished by comparing the obtained numerical results (with TPM and SPM methods) with Dudley et al. [34] experimental data, and also with Kaloudis et al. [55] numerical results (TPM method) having same boundary condition and geometrical aspect (when nanofluid is working fluid).

Described comparisons are shown in Fig. 4. One can conclude that a very good agreement exists between the present results and used numerical results [55] and empirical data [34] with TPM and SPM methods. It is concluded that obtained results by TPM method in the current investigation leads to a closer results with the available experimental data.

### Results and discussion

The difference between the obtained results employing the TPM and SPM methods for N.PTC and C.PTC are presented in the first step of current section. Utilizing the acentric tube and insulator roof considering its detail are the next step. In this step, the geometrical parameters effects on the heat transfer and fluid flow are inspected. The value of volume fraction and nanoparticles diameter in optimum condition will be present in the last step.

### TPM and SPM methods results comparison

The authors of present investigation prepared the mid-length cross-section streamlines and temperature distribution (see Fig. 3) for C.PTC having a nanofluid considering volume fraction equal to 1% at Re = 2985.9 in earlier published investigation, [31]. The annulus-air zone temperature distribution of PTC shows that the air temperature using TPM method is greater than that of the temperature using SPM method. Also, the HTF zone and absorber tube zone temperature distribution of PTC are similar in behavior. But, the annulus-air zone streamlines of PTC shows identical results in terms of flow velocity employing the TPM and SPM methods. Furthermore, the natural convection mode are detected employing the TPM and SPM methods, where two eddies are observed in the annulus zone. Further observation shows that the temperature distribution adjacent to the bottom wall is greater than that the upper walls. Referred comportment is due to the higher volume fraction near the bottom wall. Also, in this state, the natural convection is ignored, and the convection heat transfer is placed in the forced convection regime. In the mid-length cross-section nanoparticles distribution of PTC employing the TPM and SPM methods having the nanofluid, it is observed that the mid-length cross section alumina nanoparticles distribution have non-uniform distribution.

In addition, the nanoparticles distribution adjacent to the bottom wall is greater than other zone due to existence of gravity force. Higher nanoparticle concentration adjacent to the bottom wall leads to greater nanofluid thermal conductivity in the zone adjacent the bottom wall.

As it is cited, in the referred investigation, [34], the mid-length cross-section temperature distribution and streamlines of N.PTC having the nanofluid considering volume fraction of 1% and Re = 2, 985.9, acentric value of 0, and $arc-angle of 90°$ are presented. Presented results show that the SPM method provides air temperature lower than the TPM method. Also, this behavior is observed in the HTF zone and absorber tube. But, the insulated-annulus-air zone streamlines are same employing the TPM and SPM methods. As it is observed, a large eddy produces on the east-side of the annulus that is a reason for existence of pure natural convection using both TPM and SPM methods. It is observed that, the west-side of the annulus has a lower temperature than the east side. This comportment is due to existence of the west–east wind that produce more heat losses in the west portion of the annulus.

**Fig. 6** Influences of insulator arc-angles on **a** Nusselt number, **b** pressure drop, **c** mean friction factor, **d** PEC, **e** PTC outlet temperature, and **f** overall collector efficiency, with Reynolds number for the N.PTC ($\Lambda = 0$mm) having nanofluid ($d_{np} = 20$mm and $\phi = 1\%$) predicted by TPM
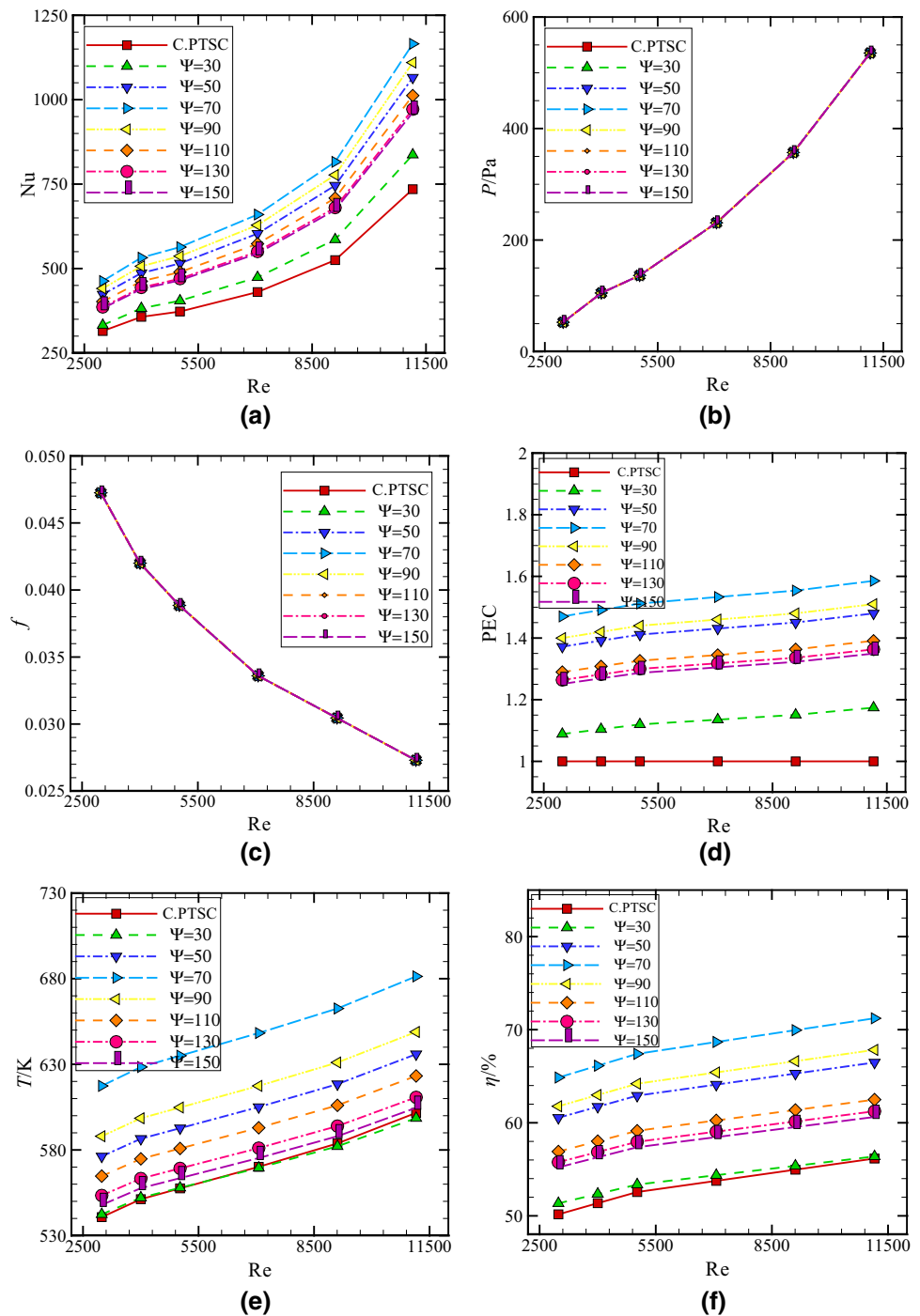


As it is observed, the temperature neighboring to the bottom wall is greater than the temperature neighboring to the upper walls. This comportment is due to existence of higher nanoparticles volume fraction neighboring to the bottom wall. Moreover, it is observed the mid-length cross-section nanoparticles distribution of PTC is non-uniform, and the higher volume fraction neighboring the bottom wall is due to existence of gravity force.

Figure 5 shows the influences of employing the TPM and SPM methods on the Nusselt number, pressure drop, … versus Reynolds number for N.PTC and C.PTC (considering acentric value of 0, and arc–angle of 90°) having the nanofluid (considering the nanoparticles volume fraction of 1% and nanoparticle diameter equal to 20nm). As it is observed in Fig. 5a, as the Reynolds number increases, the Nusselt number enhances for both C.PTC and N.PTC.

**Fig. 7** Effects of acentric values on **a** Nusselt number, **b** pressure drop, **c** mean friction factor, **d** PEC, **e** PTC outlet temperature, and **f** overall collector efficiency, with Reynolds number for the N.PTC ($\Psi = 70°$) having nanofluid ($d_{np} = 20$mm and $\phi = 1\%$) and simulated by TPM
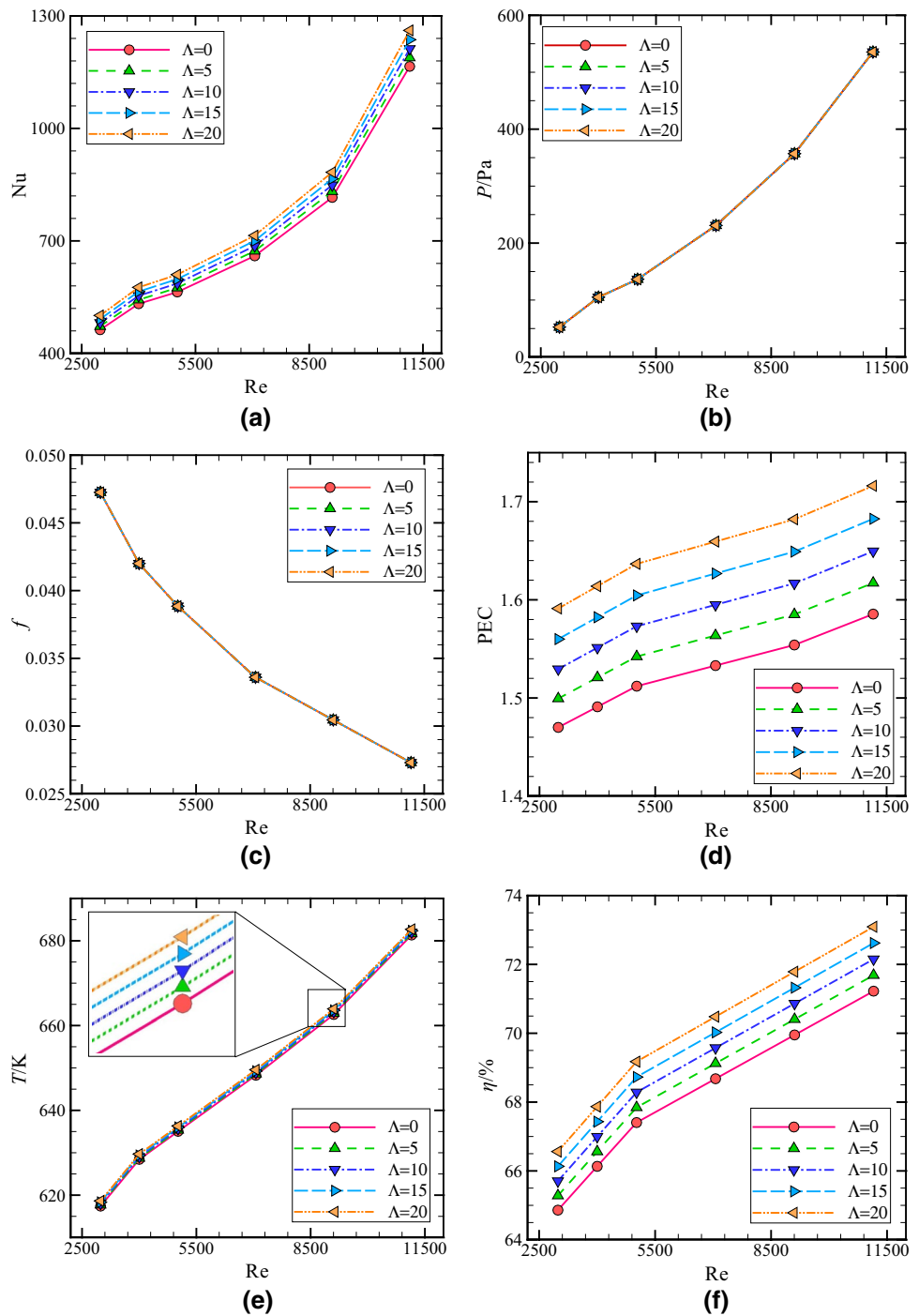


Higher Reynolds number is associated to larger velocity, which resulted in more mixing and disturbing the fluid, and consequently, heat exchange is increased. It is observed that, for C.PTC and N.PTC, obtained Nusselt number using SPM method is lower than that of TPM method. Moreover, it is observed that using the N.PTC resulted in a greater average Nusselt number than that of C.PTC, about 51% at Re = 11,151.6, and this comportment is due to existence of higher heat losses in C.PTC than that of N.PTC. The

minimum differences between employing the TPM and SPM methods (for the N.PTC and C.PTC), based on results presented in Fig. 5a, are 4.82% and 5.04%, respectively.

Figure 5b shows that the nanofluid pressure drop for the C.PTC and N.PTC have equal values. Referred comportment is due of similar wall geometry for two studied configurations. In addition, the SPM method shows the lower pressure drop at the investigated range of Reynolds number. Also, the pressure drop growths suddenly

**Fig. 8** Volume fractions effect on **a** Nusselt number, **b** pressure drop, **c** mean friction factor, **d** PEC, **e** PTC outlet temperature, and **f** overall efficiency, with Reynolds number for the N.PTC($\Lambda = 20$mm and $\Psi = 70°$) having nanofluid ($d_{np} = 20$mm) employing the TPM
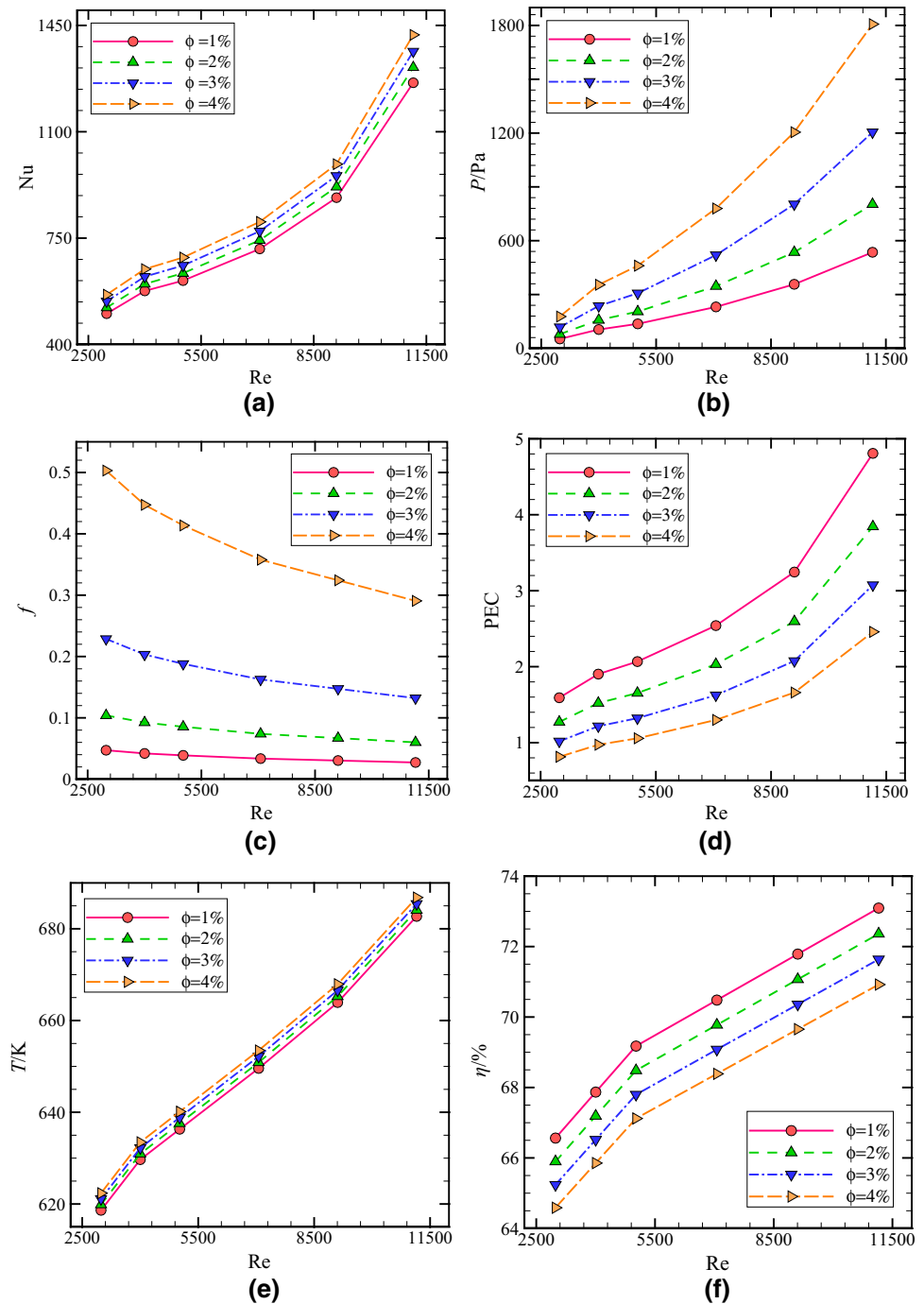
with growing Reynolds number, and this phenomenon is attributed to producing stronger vortexes. The minimum differences in pressure drop employing the TPM and SPM methods (for the N.PTC and C.PTC) in Fig. 5b are 4.97% and 4.78%, respectively.

Figure 5c illustrates that the nanofluid friction factor diminishes by growing the Reynolds number. Besides, the friction factor inside the absorber tube for the C.PTC and N.PTC have the equal values. This comportment is due to same wall geometry for two studied arrangements.

Also, as it is shown the SPM method illustrations a lower friction factor at investigated Reynolds number. The lowest differences among the friction factor using TPM and SPM methods (for the N.PTC and C.PTC) in Fig. 5c are 5.01% and 4.91%, respectively.

Figure 5d shows that, for the N.PTC, the PEC intensification with Reynolds number. The optimal Reynolds number related to Re $= 11,151.6$. It is observed that the TPM method shown the higher PEC. The nanofluid PEC with Re $= 11,151.6$ has the highest PEC for two studied

models and studied range of Reynolds number and is equal to 1.51. The lowest differences among the PEC using the TPM and SPM methods (for the N.PTC and C.PTC) in Fig. 5d are 5.05% and 4.93%, respectively. As is presented in Fig. 5e, with Reynolds number increment, the outlet temperature of nanofluid growths for investigated cases. The greater Reynolds number corresponds to the larger velocity, which resulted in more disturbing and mixing the fluid, and consequently, heat transfer is improved, and in conclusion, the outlet temperature augmented. For C.PTC and N.PTC, the outlet temperature employing the SPM method is lower than that of TPM method. Also, employing the N.PTC results in to greater outlet temperature for studied Reynolds number, and this comportment is related to higher heat losses in C.PTC than that of N.PTC. Employing the N.PTC as an alternative of C.PTC can intensification the outlet fluid (nanofluid) temperature for Re = 11, 151.6 by about 8%. The



**Fig. 9** Nanoparticles diameter effect on **a** Nusselt number, **b** pressure drop, **c** mean friction factor, **d** PEC, **e** PTC outlet temperature, and **f** overall collector efficiency, with Reynolds number for the N.PTC ($\Lambda = 20$mm and $\Psi = 70°$) having nanofluid ($\phi = 1\%$) employing the TPM
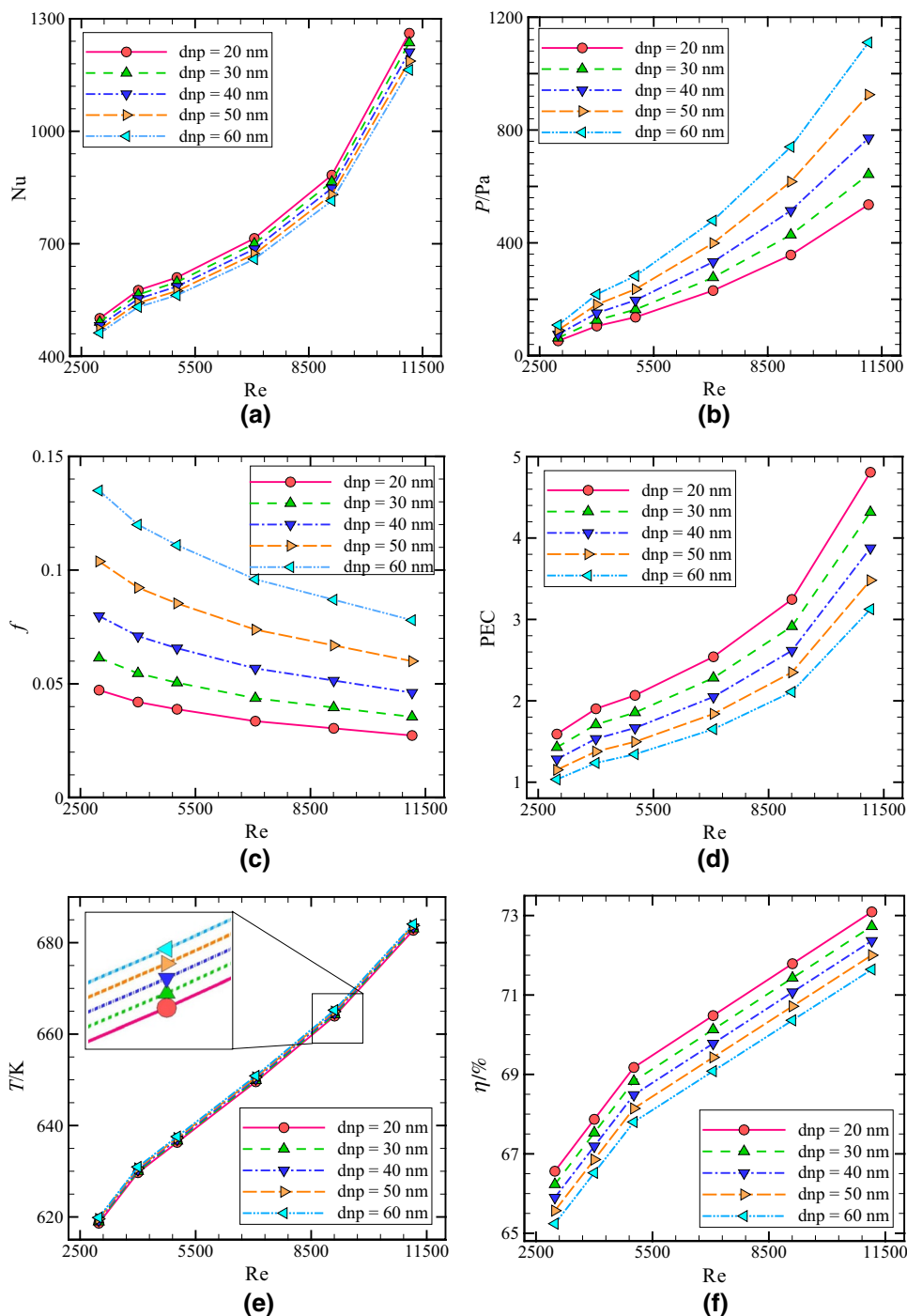
lowest differences among the outlet temperature using the SPM and TPM methods (for the N.PTC and C.PTC) in Fig. 5e are 4.77% and 4.91%, respectively. Similar behavior is observed from Fig. 5f for energy efficiency. Using the N.PTC as an alternative of C.PTC can enhance the energy efficiency for Re = 11, 151.6 by about 20%. The lowest differences among the energy efficiency using the SPM and TPM methods (for the N.PTC and C.PTC) in Fig. 5f are 4.85% and 5.00%, respectively. It is shown that employing the TPM method results in to more close results for TPM method. Consequently, in the rest of present investigation the TPM method is used to study the influence of various parameters on the interested results (pressure drop, Nusselt number and PEC).

## N.PTC geometry optimization

Figure 6 shows the influences of different insulator arc-angles values on the Nusselt number, pressure drop, … versus Reynolds number for N.PTC considering acentric value of zero having the nanofluid with nanoparticle volume fraction of 1% and nanoparticle diameter of 20nm employing the TPM method. As is displayed in Fig. 6a, with Reynolds number increment, Nusselt number enhances too for considered studied configurations.

It is showed that the PTC configuration having insulator arc-angle equal to 70° present the highest Nusselt number between studied PTC configurations, which is followed with insulator arc-angle equal to 90°, 50°, 110°, 130°, 150°, and30°, respectively. The PTC configuration having insulator arc-angle equal to 30° provide the minimum Nusselt number between studied PTC configurations and referred comportment are related to the high heat losses in referred PTC configuration. Also, the PTC configuration having insulator arc-angle equal to 150° provide a very low Nusselt number, and this results is related to the higher shading influence of insulators, which diminishes the received irradiation to the absorber tube. As is shown in Fig. 6b, it is observed that the nanofluid pressure drop inside the absorber tube has the same values for all configurations. Similar behavior is also observed in Fig. 6c for the friction factor. It is shown that this comportment is due to same wall geometry for two studied PTC configurations.

As it is observed from Fig. 6d, the behavior of PEC is same as the Nusselt number (Fig. 6a). Also, it is observed from Fig. 6e, the behavior of nanofluid outlet temperature is same as the Nusselt number (Fig. 6a).

The greater Reynolds number is due to the larger velocity value, which resulted in more mixing the fluid, and therefore, heat transfer is improved, and in conclusion, the fluid outlet temperature is enhanced.

As it is observed from Fig. 6f, the behavior of PTC energy efficiency is similar to the Nusselt number (Fig. 6a). It is shown that, for C.PTC and N.PTC, the maximum energy efficiency corresponds to Re = 11, 151.6. Consequently, in the further part of the present investigation, the N.PTC with insulator arc-angle equal to 70° is used to investigate the influence of different parameters on the results (pressure drop, Nusselt number, and PEC).

Figure 7 shows the influences of acentric characteristic on Nusselt number, pressure drop, … versus Reynolds number for the N.PTC considering the insulator arc-angle equal to 70° having the nanofluid with nanoparticle volume fraction of 1% and nanoparticle diameter of 20nm employing the TPM method. As is displayed in Fig. 7a, with Reynolds number increment, the Nusselt number enhances too for investigated PTC arrangements. It is shown that the PTC arrangement considering an acentric value equal to 20 mm provide the highest Nusselt number between studied PTC configurations, which is followed with an acentric value of 15, 10, 5, and0mm, respectively. This comportment is related to higher insulator thickness overhead the absorber tube and consequently, less heat losses in referred PTC arrangement. As is shown in Fig. 7b, it is observed that the nanofluid pressure in the absorber tube for all studied PTC configurations with the same geometric characteristics are equal. Also, similar comportment is observed in Fig. 7c for the nanofluid friction factor. It is shown that this comportment is related to the same wall geometry for two studied PTC configurations. As it is observed from Fig. 7d, the behavior of PEC is same as the Nusselt number (Fig. 7a). As is displayed in Fig. 7e, the behavior of outlet temperature is same as the Nusselt number (Fig. 7a).

As is shown in Fig. 7f, the behavior of PTC energy efficiency is similar to the Nusselt number (Fig. 7a). It is shown that, for C.PTC and N.PTC, the maximum energy efficiency corresponds to Re = 11, 151.6. Consequently, in the rest of present investigation, the N.PTC considering insulator arc-angle equal to 70° and an acentric value equal to 20mm is selected as the best geometry in the current investigation.

## Nanofluid characteristics

Figure 8 displays the influences of nanoparticles volume fractions on the Nusselt number, pressure drop, … versus Reynolds number for the N.PTC insulator arc-angle equal to 70° and an acentric value equal to 20 mm having the nanofluid with nanoparticles diameter 20mm employing the TPM method. As is presented in Fig. 8a, with Reynolds number/nanoparticles volume fraction increment, Nusselt number increases too. It is shown, the case with a volume fraction of 4, has the highest Nusselt number, which is followed by 3, 2, and1%, respectively.

Similar behavior is observed from Fig. 8b for pressure. This phenomenon is because of larger nanofluid dynamic viscosity for higher volume fractions. It is shown that the

volume fraction of 1 takes the lowest pressure drop between studied cases, which is followed by 2, 3, and 4%, respectively. Figure 8c depicts that, with Reynolds number increment, the friction factor decreases, while the friction factor increases by increasing the volume fraction. The case with volume fraction of 1 takes the lowest friction factor between all studied cases, which is followed by $\phi = 2\%, 3\%$, and 4% cases, respectively.

Figure 8d shows that the PEC for studied cases enhance with Reynolds number increment and nanoparticles volume fraction decrement. The best case is attributed to the volume fraction of 1%, followed by 2, 3, and 4%, respectively. As it is presented in Fig. 8e, with studied Reynolds number/nanoparticles volume fraction increment, the outlet temperature increases too.

The maximum outlet temperature is corresponded to the volume fraction of 4%, and it is followed by 3, 2, and 1%, respectively. As it is shown in Fig. 8f, as the studied Reynolds number growths or nanoparticle volume fraction decrease, the PTC energy efficiency enhances. Consequently, the best Reynolds number is equal to 11, 151.6, and the best volume fraction is 1%. The N.PTC energy efficiency with insulator arc-angle equal to 70° and an acentric value equal to 20 mm having nanofluid with volume fraction of 1% and nanoparticle diameter of 20 nm is equal to 73.10%.

Consequently, in the further part of present investigation, the N.PTC having insulator arc-angle equal to 70° and an acentric value equal to 20mm having nanofluid with volume fraction of 1% is selected to analyzed the nanoparticle diameters effect.

Figure 9 shows the influence of diameters on the Nusselt number, pressure drop … versus Reynolds number for N.PTC considering insulator arc-angle equal to 70° and an acentric value equal to 20 mm having nanofluid with volume fraction of 1% employing the TPM method.

As it is shown in Fig. 9a, as the Reynolds number increases or nanoparticle diameters decrease, the Nusselt number enhances. The nanoparticles diameter of $d_{np} = 20nm$ takes the maximum Nusselt number, which is followed by $d_{np} = 30nm, 40nm, 50nm$, and 60nm, respectively. As is presented in Fig. 9b, it is shown that, with the Reynolds number/nanoparticles diameter increases, the pressure drop increases. This phenomenon is attributed to higher nanofluid dynamic viscosity at higher diameters. The nanoparticles diameter of $d_{np} = 20nm$ has the lowest pressure drop, followed by $d_{np} = 30, 40, 50$, and 60nm, respectively.

Similar behavior is observed from Fig. 9c for friction factor. As it is observed from Fig. 9d, the behavior of PEC is similar to the Nusselt number (Fig. 9a), which means that the highest PEC corresponds to Re = 11, 151.6. As it is presented in Fig. 9e, with the Reynolds number/nanoparticle diameter increases, the nanofluid PTC outlet temperature

growths too. The maximum outlet temperature is associated to the nanoparticles diameter of $d_{np} = 60nm$, followed by $d_{np} = 50, 40, 30$, and 20nm, respectively. As is observed from Fig. 9f, the behavior of the PTC energy efficiency is similar to the Nusselt number (Fig. 9a). For both N.PTC and C.PTC, the maximum energy efficiency corresponds to Re = 11, 151.6 and $d_{np} = 20nm$.

The N.PTC energy efficiency with insulator arc-angle equal to 70° and an acentric value equal to 20mm having the nanofluid with volume fraction of 1%, and nanoparticle diameter equal to 20nm is equal to 73.10% and this is the highest energy efficiency in the current investigation.

## Conclusions

In the current study, the nanofluid flow characteristics and heat transfer features inside a novel parabolic trough collector (N.PTC) with insulator roof and acentric absorber tube employing a two-phase mixture model (TPM) method are simulated numerically. For both conventional and novel parabolic trough collectors, the Nusselt number, friction factor, pressure drop, PEC index, outlet temperature, and energy efficiency employing the two-phase mixture model are greater than that of the single-phase mixture (SPM) method. Employing the novel parabolic trough collector shows higher Nusselt number, outlet temperature, PEC index, and energy efficiency, with studied Reynolds numbers. The energy efficiency of N.PTC with insulator arc-angle equal to 70° and an acentric value equal to 20mm having the nanofluid with volume fraction of 1%, and nanoparticles diameter equal to 20nm is equal to 73.10% and is the highest energy efficiency in the current investigation.

## References

1. Shahzad Nazir M, Shahsavar A, Afrand M, Arıcı M, Nižetić S, Ma Z, Öztop HF. A comprehensive review of parabolic trough solar collectors equipped with turbulators and numerical evaluation of hydrothermal performance of a novel model. Sustain Energy Technol Assess. 2021;45: 101103.
2. Bayrak F, Oztop HF, Hepbasli A. Energy and exergy analyses of porous baffles inserted solar air heaters for building applications. Energy Build. 2013;57:338–45.
3. Salgado Conrado L, Rodriguez-Pulido A, Calderon H. Thermal performance of parabolic trough solar collectors. Renew Sustain Energy Rev. 2017;67:1345–59.
4. Ram Kumar P, Ravi KK. Two-fluid modeling of direct steam generation in the receiver of parabolic trough solar collector with non-uniform heat flux. Energy. 2021;226: 120308.
5. Ktistis PK, Agathokleous RA, Kalogirou SA. Experimental performance of a parabolic trough collector system for an industrial process heat application. Energy. 2021;215(Part A):119288.
6. Liu P, Dong Z, Xiao H, Liu Z, Liu W. Thermal-hydraulic performance analysis of a novel parabolic trough receiver with double tube for solar cascade heat collection. Energy. 2021;219:119566.

7. Salameh T, El Haj AM, Tawalbeh M, Ghenai C, Merabet A, Öztop HF. Analysis of cooling load on commercial building in UAE climate using building integrated photovoltaic façade system. Sol Energy. 2020;199:617–29.

8. Zaboli M, Mousavi Ajarostaghi SS, Saedodin S, Kiani B. Hybrid nanofluid flow and heat transfer in a parabolic trough solar collector with inner helical axial fins as turbulator. Eur Phys J Plus. 2021;136:841. https://doi.org/10.1140/epjp/s13360-021-01807-z.

9. Haran VH, Venkataramaiah P. Performance analysis of solar parabolic collector using $Al_2O_3$ nanofluids. Eur Phys J Plus. 2021;136:366. https://doi.org/10.1140/epjp/s13360-021-01314-1.

10. Tahari M, Ghorbanian A, Hatami M, Jing D. Physical effect of a variable magnetic field on the heat transfer of a nanofluid-based concentrating parabolic solar collector. Eur Phys J Plus. 2017;132:549. https://doi.org/10.1140/epjp/i2017-11813-1.

11. Khan S, Iqbal MS, Mehmood A. Entropy generation in mixed convection flow past a vertical wavy surface. Eur Phys J Plus. 2020;135:111. https://doi.org/10.1140/epjp/s13360-019-00027-w.

12. Hong K, Yang Y, Rashidi S, Yu G, Qingang X. Numerical simulations of a Cu–water nanofluid-based parabolic-trough solar collector. J Therm Anal Calorim. 2021;143:4183–95. https://doi.org/10.1007/s10973-020-09386-4.

13. Vijayan G, Shantharaman PP, Senthil R, Karunakaran R. Thermal performance analysis of a low volume fraction $Al_2O_3$ and deionized water nanofluid on solar parabolic trough collector. J Therm Anal Calorim. 2022;147:753–62. https://doi.org/10.1007/s10973-020-10313-w.

14. Benabderrahmane A, Benazza S, Laouedj S, Solano JP. Numerical analysis of compound heat transfer enhancement by single and two-phase models in parabolic through solar receiver. Mechanika. 2017;23(1):55–61.

15. Osorio JD, Rivera-Alvarez A. Performance analysis of parabolic trough collectors with double glass envelope. Renew Energy. 2019;130:1092–107.

16. Khosravi A, Malekan M, Assad MEH. Numerical analysis of magnetic field effects on the heat transfer enhancement in ferrofluids for a parabolic trough solar collector. Renew Energy. 2019;134:54–63.

17. Liu P, Zheng N, Liu Z, Liu W. Thermal-hydraulic performance and entropy generation analysis of a parabolic trough receiver with conical strip inserts. Energy Convers Manag. 2019;179:30–45.

18. Sadeghi G, Safarzadeh H, Ameri M. Experimental and numerical investigations on performance of evacuated tube solar collectors with parabolic concentrator. applying synthesized $Cu_2O$/distilled water nanofluid. Energy Sustain Dev. 2019;48:88–106.

19. Wang Q, Yang H, Huang X, Li J, Pei G. Numerical investigation and experimental validation of the impacts of an inner radiation shield on parabolic trough solar receivers. Appl Therm Eng. 2018;132:381–92.

20. Yang H, Wang Q, Huang X, Li J, Pei G. Performance study and comparative analysis of traditional and double-selective-coated parabolic trough receivers. Energy. 2018;145:206–16.

21. Al-Ansary H, Zeitoun O. Numerical study of conduction and convection heat losses from a half-insulated air-filled annulus of the receiver of a parabolic trough collector. Sol Energy. 2011;11:3036–45.

22. Hanafizadeh P, Ashjaee M, Goharkhah M, Montazeri K, Akrama M. The comparative study of single and two-phasemodels for magnetite nanofluid forced convection in a tube. Int Commun Heat Mass Transf. 2015;65:58–80.

23. Amani M, Amani A, Kasaeian A, Mahian O, Yan WM. Two-phase mixture model for nanofluid turbulent flow and heat transfer: effect of heterogeneous distribution of nanoparticles. Chem Eng Sci. 2017;167:135–44.

24. Kumar V, Sarkar J. Two-phase numerical simulation of hybrid nanofluid heat transfer in minichannel heat sink and

25. Khosravi-Bizhaem H, Abbassi A. Effects of curvature ratio on forced convection and entropy generation of nanofluid in helical coil using two-phase approach. Adv Powder Technol. 2018;29(4):890–903.

26. Alsarraf J, Moradikazerouni A, Shahsavar A, Afrand M, Salehipour H, Tran MD. Hydrothermal analysis of turbulent boehmite alumina nanofluid flow with different nanoparticle shapes in a minichannel heat exchanger using two-phase mixture model. Physica A. 2019;520:275–88.

27. Mohammed HA, Abuobeidab IAMA, Vuthaluru HB, Liua S. Two-phase forced convection of nanofluids flow in circular tubes using convergent and divergent conical rings inserts. Int Commun Heat Mass Transf. 2019;101:10–20.

28. Barnoon P, Toghraie D, Eslami F, Mehmandoust B. Entropy generation analysis of different nanofluid flows in the space between two concentric horizontal pipes in the presence of magnetic field: Single-phase and two-phase approaches. Comput Math Appl. 2019;77(3):662–92.

29. Scutaru ML, Vlase S, Marin M, Modrea A. New analytical method based on dynamic response of planar mechanical elastic systems. Bound Value Problem. 2020. https://doi.org/10.1186/s13661-020-01401-9.

30. Alzahrani F, Hobiny A, Abbas I, Marin M. An eigenvalues approach for a two-dimensional porous medium based upon weak, normal and strong thermal conductivities. Symmetry. 2020;12(5):848. https://doi.org/10.3390/sym12050848.

31. Abbasian Arani AA, Monfaredi F. Energy and exergy analyses of nanofluid-filled parabolic trough solar collector with acentric absorber tube and insulator roof. J Therm Anal Calorim. 2021;145:787–816. https://doi.org/10.1007/s10973-020-10267-z.

32. Abbasian Arani AA, Monfaredi F. Two-phase nanofluid flow simulation with different nanoparticle morphologies in a novel parabolic trough solar collector equipped with acentric absorber tube and insulator roof. J Braz Soc Mech Sci Eng. 2020;42:630.

33. Sadripour S. 3D numerical analysis of atmospheric-aerosol/carbon-black nanofluid flow within a solar air heater located in Shiraz. Iran Int J Num Methods Heat Fluid Flow. 2019;29(4):1378–402.

34. Dudley V, Kolb G, Sloan M, Kearney D (1994) SEGS LS2 Solar Collector Test Results. Report of Sandia National Laboratories. Report No. 94-1884

35. Corcione M. Empirical correlating equations for predicting the effective thermal conductivity and dynamic viscosity of nanofluids. Energy Conversion Management. 2011;52:789–93.

36. Keblinski P, Phillpot SR, Choi SUS, Eastman JA. Mechanisms of heat flow in suspensions of nano-sized particles (nanofluids). Int J Heat Mass Transf. 2002;45:855–63.

37. Incropera FP, Dewitt DP, Bergman TL, Lavine AS. Fundamentals of heat and mass Transfer, 6th Ed., John Wiley & Sons, 2006.

38. Chandra YP, Singh A, Mohapatra SK, Kesari JP, Rana L. Numerical optimization and convective thermal loss analysis of improved solar parabolic trough collector receiver system with one sided thermal insulation. Sol Energy. 2017;148:36–48.

39. Padilla RV, Demirkaya G, Goswami DY, Stefanakos E, Rahman MM. Heat transfer analysis of parabolic trough solar receiver. Appl Energy. 2011;88:5097–110.

40. Gnielinsli V. Heat transfer coefficients for turbulent flow in concentric annular ducts. Heat Transfer Eng. 2009;30(6):431–6.

41. Schlunder EU. Heat exchanger design handbook, Hemisphere Publication C1orporation 4 1983.

42. Siegel R, Howell JR. Thermal radiation heat transfer. New York: McGraw-Hill; 1971.

experimental validation. Int Commun Heat Mass Transf. 2018;91:239–47.

43. Dushman S. Scientific foundations of vacuum technique, John Wiley & Sons, 1962.
44. Kakat S, Shah PK, Aung W. Handbook of single-phase convective heat transfer. New York: John Wiley & Sons; 1987.
45. Hejazian M, Moraveji MK, Beheshti A. Comparative study of Euler and mixture models for turbulent flow of Al2O3 nanofluid inside a horizontal tube. Int Commun Heat Mass Transfer. 2014;52:152–8.
46. Goktepe S, Atalk K, Ertrk H. Comparison of single and two-phase models for nanofluid convection at the entrance of a uniformly heated tube. Int J Therm Sci. 2014;80:83–92.
47. Schiller L, Naumann A. A drag coefficient correlation. Z Ver Dtsch Ing. 1935;77:318–20.
48. He SL, Xiao J, Cheng ZD, Tao YB. A MCRT and FVM coupled simulation method for energy conversion process in parabolic trough solar collector. Renew Energy. 2011;36:976–85.
49. Cheng Z, He Y, Xiao J, Tao Y, Xu R. Three-dimensional numerical study of heat transfer characteristics in the receiver tube of parabolic trough solar collector. Int Commun Heat Mass Transfer. 2010;37:782–7.
50. Sokhansefat T, Kasaeian A, Kowsary F. Heat transfer enhancement in parabolic trough collector tube using Al2O3/synthetic oil nanofluid. Renew Sustain Energy Rev. 2014;33:636–44.
51. Khakrah HR, Shamloo A, Kazemzadeh Hannani S. Determination of parabolic trough solar collector efficiency using nano-fluid: a comprehensive numerical study. J Solar Energy Eng. 2017; 139(5): 051006–6–11.
52. Khakrah HR, Shamloo A, Kazemzadeh HS. Exergy analysis of parabolic trough solar collectors using $Al_2O_3$/synthetic oil nanofluid. Sol Energy. 2018;173:1236–47.
53. Wang Q, Hu M, Yang H, Cao J, Li J, Su Y, Pei G. Energetic and exergetic analyses on structural optimized parabolic trough solar receivers in a concentrated solar–thermal collector system. Energy. 2009;171:611–23.
54. Fan M, Liang H, You S, Zhang H, Zheng W, Xia J. Heat transfer analysis of a new volumetric based receiver for parabolic trough solar collector. Energy. 2018;142:920–31.
55. Kaloudis E, Papanicolaou E, Belessiotis V. Numerical simulations of a parabolic trough solar collector with nanofluid using a two-phase model. Renew Energy. 2016;97:218–29.